Development of a Full-Body Human FE Model for Pedestrian Crash Reconstructions

Yukou Takahashi, Hiroyuki Asanuma, Toshiyuki Yanaoka

Abstract The goal of this study is to develop a full-body human Finite Element (FE) model with the enhanced biofidelity and the numerical robustness necessary for use in dynamic car–pedestrian accident reconstructions in various impact scenarios. An FE model for the pelvis and lower limbs in a standing position developed in our past study was combined with FE models for bones and ligaments in the upper body taken from an occupant model. The biofidelity of the combined model was further enhanced and validated against experiments. Each body region of the full-body model was validated in multiple loading conditions, including neck bending, thoracic impact, isolated pelvis impact, thigh and leg bending, knee bending, knee ligament tension, and ankle joint rotation. The full-body model was subjected to lateral and frontal impacts at 70 km/h against a simplified car model representing a stiff front-end structure, showing that the model is robust enough to simulate high speed impacts in different pedestrian orientations.

Keywords biofidelity, human model, pedestrian, numerical robustness

I. INTRODUCTION

Crash simulations using a human Finite Element (FE) model representing a pedestrian in multiple car–pedestrian accident scenarios are one of the most effective means to investigate car–pedestrian interaction, quantify dynamic loadings to the pedestrian and predict probability of fatality or injury. This process is essential to evaluate real-world relevance of pedestrian safety technologies, including active and passive safety measures. The currently used subsystem test procedure to evaluate pedestrian passive safety performance was originally developed by the European Enhanced Vehicle-safety Committee (EEVC) [1] and essentially assumes lateral impact of a car to a pedestrian at 40 km/h. Due to the representation of pedestrian accidents with particular impact scenarios, it is not possible to accurately estimate the real-world effectiveness of passive safety measures evaluated by such a test procedure based solely on the test results. It needs to be investigated against various impact configurations seen in actual car–pedestrian accidents in order to predict reduction in pedestrian fatalities and casualties expected to be provided by the measure in real-world accidents. The recent advancement of active safety technologies would change the distribution of impact speeds as a result of the activation of systems for crash avoidance. The prediction of the combined effect of both active and passive safety measures on the reduction of pedestrian fatalities and casualties also requires prediction of car–pedestrian interactions at various impact configurations. Fredrikson et al. [2] investigated 54 pedestrian accidents from the German In-depth Accident Study (GIDAS) database, occurring from 1999 to 2008 and with AIS3+ head injuries, and estimated isolated and combined effects of specific active and passive safety measures on head injury mitigation. The study used a particular function between the impact speed and the probability of AIS3+ head injury to estimate the effect of the measures, which assumes that the injury probability is solely dependent on the impact speed. This assumption may not apply if the impact speed distribution is significantly different between urban and rural areas where the distribution of car–pedestrian impact configurations would be significantly different. These issues can be taken into consideration when all the different impact configurations in the real-world accidents are dynamically reproduced by car–pedestrian impact simulations using a human model.

Accurate predictions of the probability of injuries in multiple accident scenarios by means of impact simulations using a human FE model would require the biofidelity of the human model. The Global Human Body Models Consortium has developed a detailed and extensively validated human FE model for a seated occupant

Y. Takahashi is Chief Engineer (tel: +81-28-677-3311, fax: +81-28-677-7500, e-mail: yukou_takahashi@n.t.rd.honda.co.jp), H. Asanuma is Engineer and T. Yanaoka is Assistant Chief Engineer at Honda R&D Co., Ltd. Automobile R&D Center, Japan.

by representing whole-body skeletal and soft tissues. However, a detailed pedestrian model in a standing position is still needed to be developed in a future stage [3]. Watanabe et al. [4] developed a full-body human FE model representing a pedestrian with a primary focus on brain and internal organ injuries. However, the result of 4-point knee bending validation is the only information provided for the lower limb model validation. In a previous study, the authors developed a human FE model with the upper body represented by articulated rigid bodies and the pelvis and lower limbs modeled by finite elements to investigate pelvis and lower limb interactions with a car front-end structure in car–pedestrian impacts [5-6]. Since the upper body is modeled by articulated rigid bodies representing only the external surface, it was not possible to predict injuries to the upper body such as rib fractures or abdominal injuries. The ankle joint is represented by one single mechanical joint element, which would require biofidelity improvement when ankle joint injuries are to be predicted. The knee model was validated in pure (4-point) lateral bending. Although the primary loading to the knee in pedestrian crashes would be lateral bending, the knee is also subjected to shear loading and thus additional validation in combined loading would be needed. The bending response of the lower limb model was validated for individual long bones (femur, tibia and fibula) and assembly (thigh and leg). This ensured biofidelic overall bending response of the leg assembly, however the distribution of the loads transmitted by the tibia and the fibula has not been clarified. In addition to the biofidelity improvement of the model, it is also necessary to make sure that the model is robust enough to survive severe impacts from a car that need to be simulated to estimate real-world relevance of safety technologies by means of computer simulations of car–pedestrian crashes.

The goal of the study is to develop a human FE model in a standing position that will ultimately be capable of predicting probability of major injuries to a pedestrian whole body in various impact configurations. This study developed a full-body human FE model in a standing position by combining the FE upper body model taken from Dokko et al. [7] with the pelvis and lower limb FE model developed by the authors [5-6]. Some modifications were made to the knee, leg and ankle for improved biofidelity. The neck, thorax, pelvis, thigh, knee, leg and ankle were validated against experimental data to validate the components of the modified full-body model. The model validation included 3-point bending of the knee and the bending response of the ankle, which have not been conducted in former studies [5-6]. The model was subjected to lateral and frontal impacts from a simplified car model representing a stiff front-end structure at 70 km/h, in order to evaluate the numerical robustness of the model.

II. METHODS

The combined FE whole body model was further modified from two different viewpoints: one to enhance the biofidelity of the model; and the other to improve the numerical robustness of the model in high-speed collisions. The components of the modified model were re-validated against experimental data due to the modifications made. The 3-point bending of the knee and the ankle rotation were added to the validation for enhanced biofidelity. The numerical robustness of the model was evaluated in lateral and frontal collisions. The lateral impact was used to represent the impact configuration most frequently seen in car–pedestrian accidents. The frontal impact was employed to investigate the effect of the musculature around the knee on the resistance to hyperextension of the knee.

Full-body Pedestrian Model

The upper part of the whole body human FE model in a seated position developed by Dokko et al. [7], representing the shape of the rib cage for 35 years old, was combined with the pelvis and lower limb human FE model in a standing position developed by the authors [5-6] at the T12-L1 joint. The spine curvature was not changed. Both models have been developed in PAM-CRASH. As opposed to the size of the pelvis model scaled to 50th percentile American male [5-6], the rib cage model was based on CT scans from a particular individual [8]. Although the bell-shaped rib cage of the baseline model can be viewed as part of individual variations, the width of the bottom of the rib cage was much larger than the width of the pelvis scaled to 50th percentile male. Since the protrusion of the bottom of the rib cage may predict unrealistic rib fracture mechanism, it was decided to morph the shape of the rib cage to match the contours of the rib cage in frontal and lateral views presented in the published rib cage anatomy figures [9]. Figure 1 presents the modified full-body human FE model in a standing position, along with the comparison of the shape of the rib cage relative to the pelvis. Since the biofidelity of the head of the occupant model has not been validated, the model was replaced with the head from the FE pedestrian dummy model developed by Takahashi et al. [10] and Shin et al. [11]. The dummy head model does not represent the brain, and its acceleration response has been validated against the head drop test where the dummy head is dropped onto a rigid surface as described in the NHTSA validation materials [12].

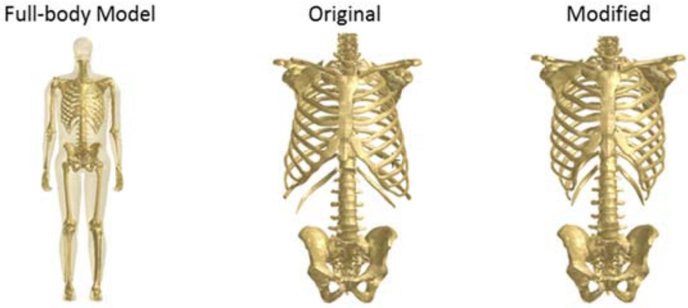

Fig. 1. Full-body FE human model in a standing position and comparison of original and modified rib cage.

Model Modification

Further modifications were made to the full-body FE human model in a standing position, presented in Fig. 1, to further enhance its biofidelity and ensure numerical robustness of the model in high-speed impacts.

Biofidelity: modifications were made to the knee, the leg and the ankle of the model. In the original model, an isotropic solid material model is used for three out of the four knee ligaments (Anterior and Posterior Cruciate Ligaments; ACL and PCL, Lateral Collateral Ligament; LCL). In addition, an isotropic shell material model is used for the knee joint capsule. For these reasons, the ligaments and the joint capsule are allowed to generate compressive loads, which may result in unrealistic knee behavior. Since these components consist of the fibers bundled by the matrix and the majority of the load is transmitted through the fibrous tissues, which essentially do not bear compressive loads, the material properties of the solid and the shell elements were switched to those representing the property of the ligament matrix, and the fibers were represented by tension-only bar elements that run along the mesh lines of the solid and the shell elements, as presented in Fig. 2. As in the original model, the cruciate ligaments are divided into anterior and posterior bundles (anterior ACL/PCL; aACL/aPCL, posterior ACL/PCL; pACL/pPCL). Since the Medial Collateral Ligament (MCL) of the original model is represented by shell elements due to the small thickness, the MCL model was unchanged because the compressive force generated by this ligament was not significant. Due to insignificance of the contribution from the collagen matrix to the tensile property of a ligament, the linear elastic material was used and the elastic modulus of 1.6 MPa and the Poisson's ratio of 0.4 were applied by referring to Hadjipanayi et al. [12], Susilo et al. [14] and Lewis et al. [15].

The connection between the tibia and the fibula of the original model is provided by a rigid-body constraint defined at the proximal and distal ends of the fibula. Although the overall response of the leg complex has been validated in 3-point bending against experimental data, the distribution of load transmission between these two bones may be influenced by this unrealistic definition of the connection between them. For this reason, the rigid body constraints were eliminated, and the interosseous membrane was modeled using shell elements and the tibiofibular ligaments at the proximal and distal ends were modeled using tension-only bar elements as illustrated in Fig. 3. Due to the lack of information on the interosseous membrane, the elastic modulus of 3.35 MPa estimated from Bertram et al. [16] was applied to a linear elastic material model, and the same thickness as that used for the knee joint capsule was specified. The material property of the tibiofibular ligaments was determined so that biofidelic load distribution between the tibia and the fibula is obtained in the model validation.

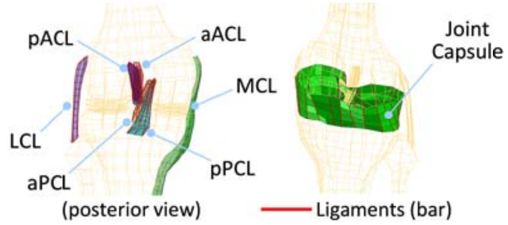

Fig. 2. Modified knee ligament models.

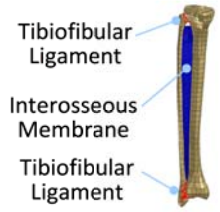

Fig. 3. Modified leg model (without flesh).

For simplification, the ankle of the original model was represented by one single joint element because the model focused on the leg and above. Although leg fractures are more common, ankle fractures are not uncommon in pedestrian crashes. Thus, it was decided to modify the ankle joint model. Figure 4 presents the structure of the modified ankle joint. The talus and the calcaneus were modeled as rigid bodies, and the external surface of the foot was included in the rigid body definition of the calcaneus. The ankle model was modified to incorporate two different joints represented by joint elements: the talocrural joint, connecting the bottom of the leg and the talus; and the subtalar joint, connecting the talus and the calcaneus. The rotational degrees of freedom (DOF) in dorsiflexion/plantarflexion and internal/external rotation were defined at the talocrucal joint, and the rotational DOF in inversion/eversion was given to the subtalar joint. The major ligaments around the ankle joint, such as the talofibular ligament, the deltoid ligament and the calcaneofibular ligament, were represented by the tension-only bar elements. The profile of the force-strain response of these ligament models was taken from the knee ligament model and the magnitude was determined so as to match the overall rotational response of the ankle.

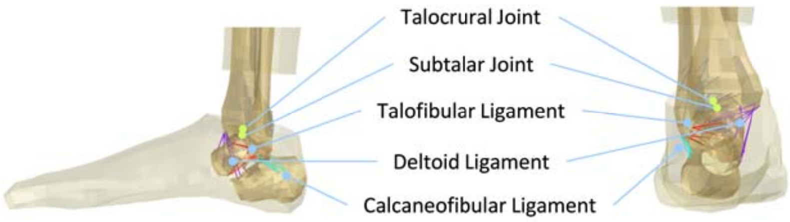

Fig. 4. Modified ankle joint model.

Numerical robustness: the Japanese accident statistics for 2013, from the Institute for Traffic Accident Research and Data Analysis (ITARDA) [17], show that 99.7% of pedestrian accidents against passenger cars occurred at the car travel speed of 70 km/h or lower. This led to the requirement of the maximum impact speed of 70 km/h, at which the numerical robustness of the model needs to be guaranteed so that the model can be used to reconstruct the entire distribution of different impact conditions.

In the original model, the glenohumeral (shoulder) joint and the elbow joint are modeled using ligament constraints without specifying any joint elements. Preliminary impact simulations at high speeds frequently showed the dislocation of the shoulder and the elbow joints. In order to ensure the numerical robustness of the model up to 70 km/h, it was necessary to define joint elements at these joint locations to eliminate the dislocation, which was found to cause numerical instability. Since the ligament models around these joints in the original model were unchanged, the additional joint elements only provided constraints in translation. The radiocarpal (wrist) joint originally modeled using a joint element remained unchanged.

The cervical, thoracic and lumbar vertebrae of the original model are defined as rigid bodies, with the response characteristics of intervertebral discs lumped into joint elements, and the contact definitions are specified between each pair of the neighboring vertebrae. Due to the rigid-rigid contact beyond the range of motion of the vertebral column, preliminary impact simulations at high speeds showed a significant high-frequency vibration of the head acceleration. Since such a vibration makes it difficult to predict probability of injuries to those body regions, the contact definitions between neighboring vertebrae were eliminated. Alternatively, a stiff region was added to the moment-angle property of the joint element specified at the center of the vertebral disc beyond the range of motion. The range of motion was determined from the model in flexion/extension, lateral bending and torsion by identifying the angle corresponding to the initial contact of the neighboring vertebrae. Table I summarizes the results of the identification of the range of motion.

TABLE I
RANGE OF MOTION OF VERTEBRAE

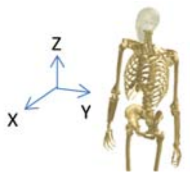

Axis of Rotation	Range of Motion (deg)														
	Head-C1	C1-C2	C2-C3	C3-C4	C4-C5	C5-C6	C6-C7	C7-T1	T1-T12	T12-L1	L1-L2	L2-L3	L3-L4	L4-L5	L5-S1
X	±8	±0	±10	±11	±11	±8	±7	±4	±2.5	±4	±4	±4	±4	±4	±0
Y	±13	±10	±8	±13	±12	±17	±16	±9	+2.5 -3.3	±5.6	±5.6	±5.6	±5.6	±11.25	±11.25
Z	±0	±47	±9	±11	±12	±10	±9	±8	±2.5	±2.5	±2.5	±2.5	±2.5	±2.5	±2.5

The knee joint of the original model is primarily constrained by the ligaments and the joint capsule without modeling the musculature, considering its insignificant contribution in pure lateral bending. Preliminary impact simulations at high speeds revealed that the peak hyperextension of the knee reached 39.5 degrees at 70 km/h for a pedestrian facing a vehicle. Since the musculature must play a significant role in such a large hyperextension, even passively, the muscle models represented by tension-only bar elements were added to the back of the lower limb model, as shown in Fig. 5. Each of the biceps femoris, the semi-tendinosus and the semi-membranosus in the thigh and the triceps surae in the leg was respectively modeled using two pairs of tension-only bar elements in series. All of the four pairs of the bar elements were divided into two parts (the shorter part proximal to the knee and the longer part distal to the knee) running through slip rings attached to either the distal femur or the proximal tibia to eliminate the change in the direction of the tensile force along the one-dimensional bar elements due to knee bending. The actual attachment points of the added thigh and the leg muscles are on the pelvis and the calcaneus, respectively. However, as the joint characteristics of the hip and the ankle were individually validated without incorporating the effect of these muscles, the attachment points were placed at the proximal femur and the distal tibia, respectively. The bending stiffness of the knee in hyperextension was estimated from Bizot et al. [18] at 18 Nm/degree, and the force to be generated by each of the four muscle models at 20 degrees of hyperextension was determined such that the knee moment is equally distributed among the four ligament models. Figure 6 presents the stiffness characteristics of the bar elements for each of the four muscle models. In order to avoid unfavorable influence on the varus/valgus bending response, the initial stiffness was reduced and the magnitude of the elongation and the force at which the stiffness changes was determined, such that the influence of the addition of the muscle models on the varus/valgus bending moment falls within 10% based on Lloyd and Buchanan [19].

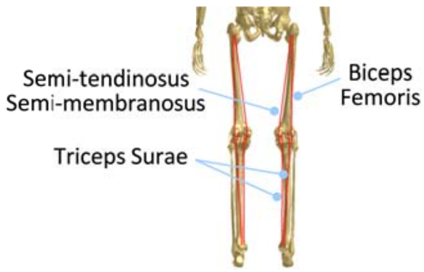

Fig. 5. Lower limb muscle models.

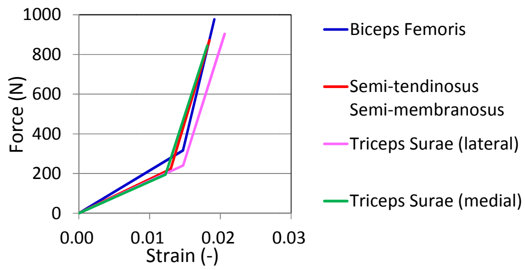

Fig. 6. Stiffness characteristics of muscle models.

Model Validation

Although the baseline models used to develop the full-FE human model representing a pedestrian have been extensively validated at the component level [5-8], the further modifications to the model require re-validation of the biofidelity of the model in the conditions where the model response may be influenced by the modification of the components.

Neck: since the bending characteristics of the joints specified at the intervertebral discs were changed for the cervical spine, the neck response in flexion and lateral bending was re-validated against the volunteer tests conducted by Ewing et al. [20] and analyzed by Thunnissen et al. [21]. The head-neck complex was taken from the full-body model and the acceleration time history from Thunnissen et al. [21] was applied to T1 in the anterior-posterior and lateral directions, as shown in Fig. 7. The bottom of the skin and the muscles was rigidly constrained and the same prescribed motion was applied. The excursion of the head CG relative to T1 was compared for both flexion and lateral bending against the corridors presented by Thunnissen et al. [21]. For the flexion, the linear acceleration in the anterior-posterior and the superior-inferior directions and the angular acceleration about the lateral axis were compared with the test results. For the lateral bending, the linear acceleration in the lateral and the superior-inferior directions and the angular acceleration about the anterior-posterior axis were compared.

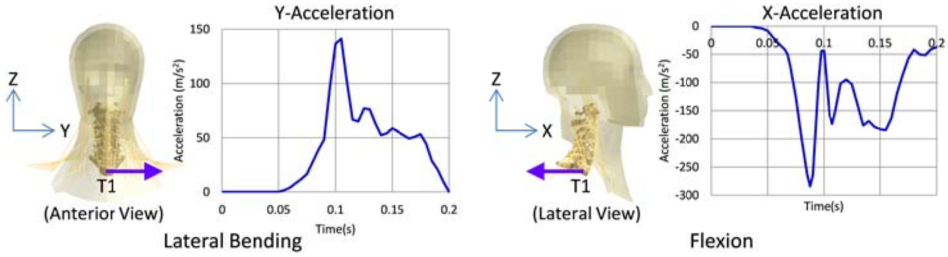

Fig. 7. Lateral bending and flexion of head-neck complex.

Thorax: the impact response of the thorax was also re-validated in frontal and oblique impactor tests because of the change in the contour of the rib cage and the modifications to the bending characteristics at the intervertebral discs. The thoracic impact test results conducted by Kroell et al. [22-23] and Viano [24] were used for the frontal impact and the oblique impact, respectively. For the frontal impact, three different impact conditions, which are summarized in Table II, were used. Due to the variations in the mass of the impactor and the impact speed, the average values of the test conditions were applied to the human model simulation. Due to the lack of the scaled data, each of the test results presented in the papers [22-23] was digitized and the time histories of the force and the thoracic deflection were scaled based on Eppinger et al. [24] using the following equations:

$$\lambda_L = \frac{H_{Subject}}{H_{Standard}} \tag{1}$$

$$F_{Scaled} = \lambda_L^2 \cdot F_{Subject} \tag{2}$$

$$D_{Scaled} = \lambda_L \cdot D_{Subject} \tag{3}$$

$$t_{Scaled} = \lambda_L \cdot t_{Subject} \tag{4}$$

where λ_L is length scale factor, $H_{Standard}$ is standard height (175.6 cm for 50th percentile male), $H_{Subject}$ is height of the subject tested, F_{Scaled} is scaled force (N), $F_{Subject}$ is force from the subject tested (N), D_{Scaled} is scaled thoracic displacement (m), $D_{Subject}$ is thoracic deflection from the subject tested (m), t_{Scaled} is scaled time (s), $t_{Subject}$ is time from the test (s). This scaling procedure assumes that the scaling factors of the mass density and the elastic modulus equal 1. For each scaled time, the average force versus the average displacement was plotted, and ellipses with the lengths of the axes representing one standard deviation of the force and the thoracic deflection were drawn. Then the upper and lower bounds of the force-deflection corridor were determined from the envelop curves. The force-deflection response from the human model simulation was compared with the force-deflection corridor for each of the impact conditions in Table II. For the oblique impact, the impact force time history corridors scaled to 50th percentile male presented in Viano [24] for the impact speeds of 4.4 m/s, 6.5 m/s and 9.5 m/s were used to compare the impact force from the human model simulations. Figure 8 illustrates the computer simulation models representing the frontal and oblique impact tests.

TABLE II

FTONTAL IMPACT CONDITIONS

Condition 1			Condition 2			Condition 3		
Test ID	M (kg)	V (m/s)	Test ID	M (kg)	V (m/s)	Test ID	M (kg)	V (m/s)
42FM	22.9	4.9	48FM	10.4	7.1	12FF	22.9	7.2
45FM	23.0	5.1	50FM	10.4	7.3	13FM	22.9	7.4
53FM	23.0	5.2	51FM	10.4	6.7	14FF	22.9	7.3
60FM	23.0	4.3	52FM	10.4	7.2	15FM	23.6	6.9
			56FM	10.4	6.9	18FM	23.6	6.7
			58FM	10.4	6.8	20FM	23.6	6.7
			62FM	10.0	6.9	21FF	23.6	6.8
						22FM	23.6	6.7
						63FM	23.0	6.9
						64FM	23.0	6.9
Ave.	22.98	4.88	Ave.	10.34	6.99	Ave.	23.27	6.95
Val.	**23.0**	**4.9**	**Val.**	**10.3**	**7.0**	**Val.**	**23.3**	**7.0**

M: Mass of impactor, V: Impact speed
Ave.: Average, Val.: Validation Condition

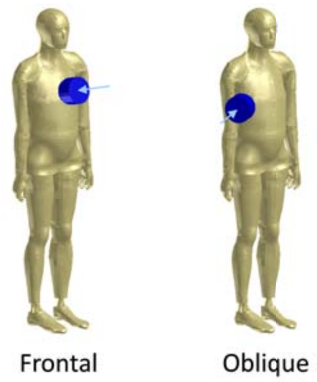

Fig. 8. Frontal and oblique thoracic impact.

Leg: the leg model was re-validated in 3-point bending due to the addition of the interosseous membrane. The leg model was subjected to dynamic mid-shaft 3-point bending at 1.5 m/s of the loading rate, as presented in Fig. 9, and the moment-deflection response was compared with that from the response corridor developed by Ivarsson et al. [26]. The effect of the addition of the interosseous membrane on the load distribution between these two bones was verified by comparing the contribution of the load born by the fibula with the values from the literature in the axial compression of the leg. The proximal end of the tibia was rigidly fixed to the inertial space and the foot defined as a rigid body was forced to displace vertically at 250 mm/min. Due to the lack of information from the literature on the exact cross-section of the leg at which the load transmission ratio was determined, three different cross-sections (mid-shaft, distal third and proximal third) of the leg were defined and the ratio was calculated in all of the three cross-sections at 1.0 kN compression. The values of the contribution of the fibula in axial compression obtained from the literature ranged from 6.0% to 17.0% (Funk et al. [27]: 6.0%; Takebe et al. [28]: 6.4%; Shuler et al. [29]: 6–17%).

Knee Ligament: the models for the ACL, PCL and LCL were individually re-validated because of the change in the structure of the model for these ligaments. The validation was conducted in dynamic tension using a bone-ligament-bone complex extracted from the knee model at the loading rates of 0.016 mm/s (quasi-static) and 1600 mm/s (dynamic). The data from Bose et al. [30] and van Dommelen et al. [31] were analyzed to develop force-deflection corridors and the average and variability of the failure points. Data scaling was not applied due to the lack of the anthropometric information on some of the subjects used in the experiment. Due to a large variability of the data between subjects, a specific procedure to develop force-deflection corridors was used. First, the average force-deflection curve was determined up to the smallest deflection at failure among the subjects, and the standard deviation in force was calculated for each deflection. Then the ratio of the force from the test with the smallest ultimate deflection to that from the test with the largest ultimate deflection was calculated and curve-fitted as a function of deflection. Then the function was used to extrapolate the ratio up to the largest ultimate deflection to estimate the average force-deflection curve up to that deflection level. The average values and the standard deflection of the force and the deflection at failure were determined directly from the test results to determine the average failure point and its variation. The average standard deviation in force was applied to determine the upper and lower bounds of the response corridors. The standard deviation in the deflection was not taken into account due to the prescribed deflection time history used by the tests [30-31]. Figure 10 presents the example of the bone-ligament-bone complex model for the dynamic tension of aACL. Material Type 202 was used for the bar elements representing the ligament fibers and non-linear rate-dependent constitutive characteristics were specified.

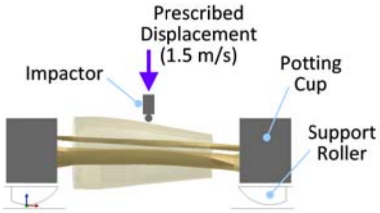

Fig. 9. 3-point bending of leg

Fig. 10. Individual knee ligament tension

Knee Joint: the knee joint model was re-validated in 4-point bending due to the change in the structure of the ligament and the knee joint capsule models. Since 4-point bending essentially provides a pure bending of the knee, the model was also validated in 3-point bending that applied a combination of the bending and shear loads, which normally takes place in actual car–pedestrian collisions. For 4-point bending, the moment-angle response in valgus bending of the knee was compared with the response corridor scaled to 50th percentile male presented in Ivarsson et al. [26]. For 3-point bending, the shear force time history was compared against Bose et al. [32]. Figure 11 presents the 3-point bending test set-up used by Bose et al. [32]. Based on the beam theory, the ratio of the valgus bending moment applied at the knee to the shear force is determined by $L - L_K$ (Fig. 11). In order to validate the knee model under the condition with relatively larger contribution of the shear force, the tests with a smaller moment-to-shear force ratio (test ID: Comb 4-8 in Bose et al. [32]) were used. One of the tests (test ID: Comb 7 in Bose et al. [32]) was omitted as an outlier. Three-point bending simulation was conducted under the moment-to-shear force ratio of 2.69, determined from the average of the four tests. Considering the use of the specimens in the tests without preconditioning the ligamentous tissues, the initial slack strain of 0.2 was applied to the ligament and knee joint capsule models.

Ankle: due to the modification of the ankle in the modified model, the moment-angle responses of the ankle in dorsiflexion/plantarflexion and inversion/eversion were compared with that from the literature. The proximal end of the tibia was rigidly fixed to the inertial space and the rigid-body foot was forced to rotate about the corresponding joints at 500 degrees/s. The moment-angle responses were compared with those from Crandall et al. [33].

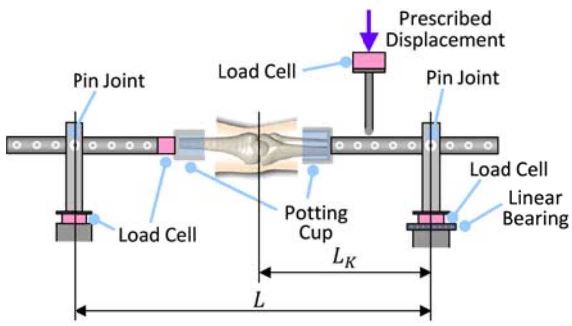

Fig. 11. 3-point knee valgus bending set-up used by Bose et al. [32].

Numerical Robustness Evaluation

The numerical robustness of the model was evaluated in an impact from a car at 70 km/h to evaluate the effect of the measures to enhance the numerical robustness. Failure representation options of the human model were turned off to provide largest-possible internal loads and evaluate the numerical robustness under the most severe conditions. A simplified car model representing a stiff car front-end structure prior to the mandate of pedestrian protection regulations and NCAPs was used for the impact simulations. The model consists of a combination of multiple rigid surfaces connected to linear spring elements representing the stiffness of the components. Unpublished legform, upper legform and headform test results against old Japanese cars without any pedestrian protection measures were analyzed to obtain the average stiffness of the lower part of the bumper, bumper, hood edge and windshield. The shape of the car model was determined from the average of 31 old Japanese cars in the sedan category prior to the compliance with the regulation for pedestrian protection. The stiffness characteristics of these components were determined from the average + 1SD. The car model represents the stiffness of the components using one-dimensional springs with non-linear stiffness characteristics, as presented by Asanuma et al. [34]. In addition to the division of the car front surface in the longitudinal direction done by the earlier study to represent the distribution of different stiffness characteristics, the car surface area was also divided in the lateral direction to represent different stiffness characteristics between the car center part and the right and left parts. Two pedestrian lower limb stances were used – upright and mid-gait cycle. Three impact simulations were conducted using the simplified car model and the modified human model. The upright model was hit by the car model laterally at 70 km/h. The mid-gait stance model was hit by a car both laterally and frontally at 70 km/h. The frontal impact simulation was conducted to clarify the effect of the addition of the musculature around the knee on the knee kinematics during a collision. Figure 12 shows the example of the car–pedestrian impact simulation for lateral impact. Figure 13 presents the stiffness characteristics of the car model for different regions along the centerline of the car.

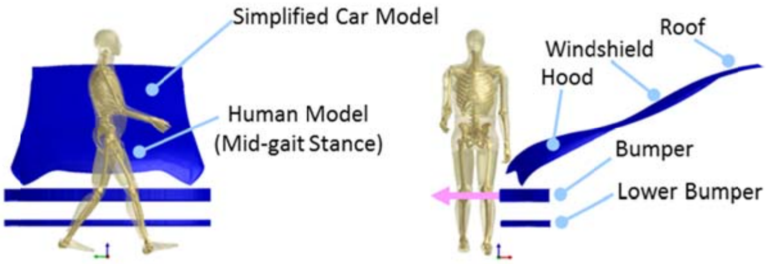

Fig. 12. Car-pedestrian impact simulation.

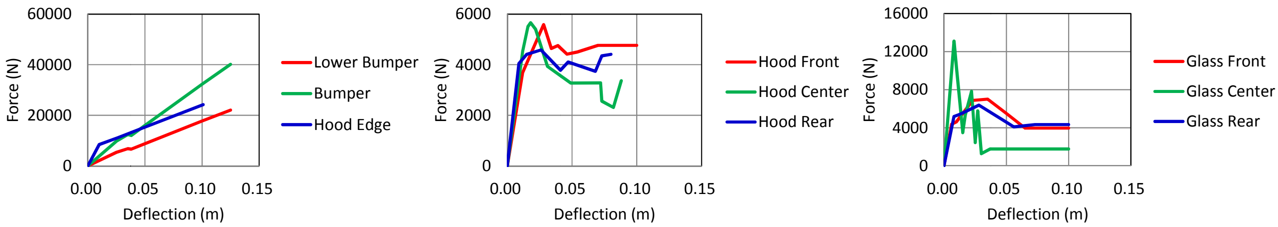

Fig. 13. Force-deflection characteristics of simplified car model.

III. RESULTS

Model Validation

Neck: Fig. A1 in the Appendix compares the human model simulation results with the test results in the lateral bending of the neck for the head CG trajectory, lateral (Y) and vertical (Z) linear acceleration of the head and angular acceleration about the frontal (X) axis. Figure A2 in the Appendix presents similar comparisons in the flexion of the neck for the head CG trajectory, frontal (X) and vertical (Z) linear acceleration of the head and angular acceleration about the lateral (Y) axis. All the accelerations are relative to the global coordinate system affixed to the inertial space.

Thorax: Fig. A3 in the Appendix compares the force-deflection response of the thorax with the scaled response corridor determined in the current study from the test results presented in Kroell et al. [22-23] for the three different combinations of the impactor mass and the impact speed shown in Table II. The thoracic deflection was determined as the displacement of the impactor relative to T9. Figure A4 in the Appendix compares the impact force time history with the scaled force time history corridor from Viano [24] for the impact speeds of 4.4 m/s, 6.5 m/s and 9.5 m/s.

Leg: Fig. A5 in the Appendix shows the comparison of the moment-deflection response in dynamic 3-point bending of the mid-shaft leg between the response corridor presented in Ivarsson et al. [26] and the modified human model. Figure 14 shows the force time history in axial compression of the leg from the modified human model simulation for the four different cross-sections. The contribution from the fibula to the overall axial force ranged from 7.3% to 16.1% at 1 kN of the total force, which are within the range from the literature.

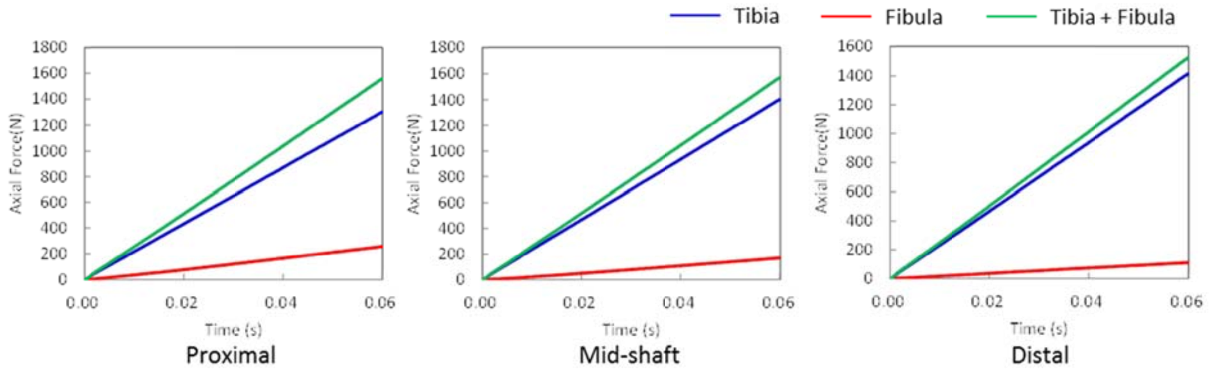

Fig. 14. Load distribution between tibia and fibula in leg compression.

Knee Ligament: Fig. A6 in the Appendix shows the comparison of the force-deflection response of individual knee ligaments at the loading rates of 0.016 mm/s and 1600 mm/s between the response corridors and failure point variations determined in this study and the results of the modified model simulations. The corridor and the failure point variation were not determined for pPCL at 0.016 mm/s because only one test was conducted.

Knee Joint: Fig. 15 compares the moment-angle response in 4-point valgus bending of the knee between the scaled response corridor from Ivarsson et al. [26] and the modified model simulation result. Figure 16 compares the shear force time history in 3-point bending of the knee between the test data from Bose et al. [32] scaled to 50th percentile male and the simulation result using the modified model.

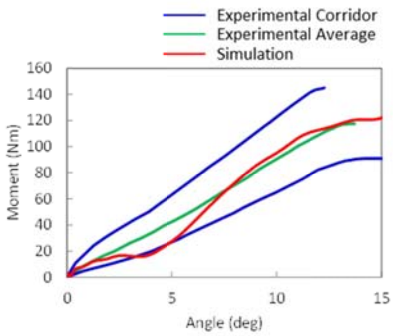

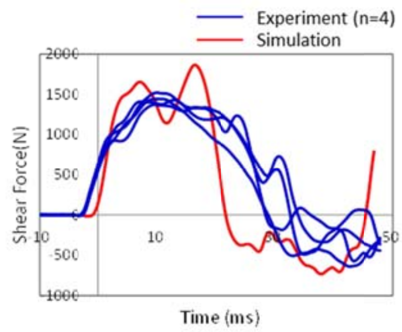

Fig. 15. Validation results of knee bending moment in 4-point valgus bending.

Fig. 16. Validation results of knee shear force in 3-point valgus bending.

Ankle: Fig. 17 shows the comparison of the moment-angle response in dorsiflexion/plantarflexion and inversion/eversion between the experiment from Crandall et al. [33] and the modified model simulation.

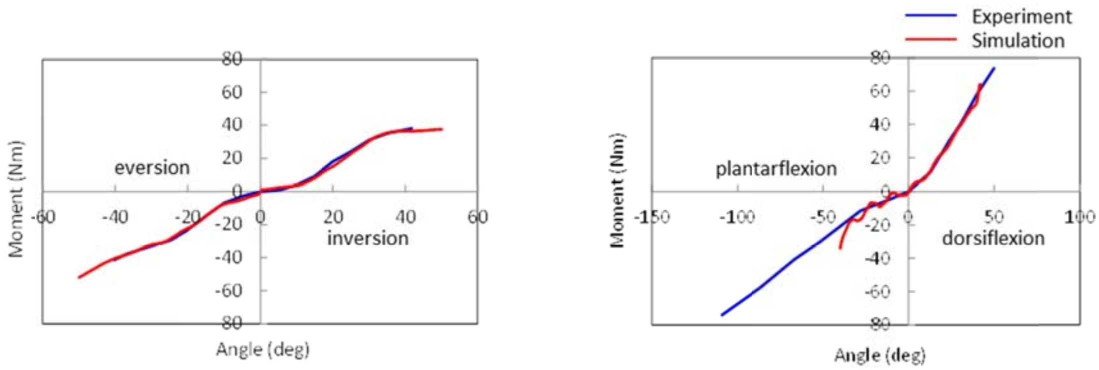

Fig. 17. Validation results of ankle joint rotation.

Numerical Robustness Evaluation

All of the three impact simulations were successfully run up to the head contact with the car model. The kinematics of the modified pedestrian model is illustrated in Fig. A7 in the Appendix for the three impact configurations.

IV. DISCUSSION

The results of the biofidelity validation generally showed that the impact response of the modified human FE model is more biofidelic at the component level, except the upper limb, for which validation was not conducted. The upper limb joint models were simplified using joint elements to ensure the numerical robustness at high-speed impacts. The elimination of the contact definitions between the rigid-body cervical and thoracic vertebrae yielded the head response without unfavorable high frequency oscillations, as shown in Fig. A1 and Fig. A2 in the Appendix. The modifications to the thorax and the ankle models, validated against experiment, allow the estimation of impact responses to these body regions. The additional validation of the knee model in 3-point bending ensured that the model is capable of predicting responses to combined bending and shear loads. The change in the ligament model structure to the bar models representing the fibers and the solid models representing the matrix eliminated unrealistic compressive load due to the use of the tension-only bar elements, while maintaining a similar level of biofidelity compared to the baseline model. Although the material property of the interosseous membrane requires validation, the validation of the load distribution between the tibia and the fibula within the leg is important when local failure of a particular bone needs to be predicted. The validation of the leg model in 3-point bending showed that the model prediction almost traced the lower bound of the experimental corridor from Ivarsson et al. [26]. However, the stiffness of the later phase of loading, where the bone resistance dominates, is similar to the experimental data. This 'shift' of the curve in deflection can be attributed to the decreased thickness of the leg flesh between the bone and the ram relative to the thickness in a standing position due to the amputated muscles hanging down the horizontally placed bone. The impact simulations at 70 km/h succeeded in calculating the kinematics of a pedestrian up to the head contact with the car without any errors terminating the computation, suggesting that the model can be used to simulate almost the entire range of the impact scenarios seen in real-world accidents in terms of the impact speed.

The knee model validations in 3-point and 4-point bending assumed the slack strain of 0.2 due to the lack of preconditioning of the ligaments in the experiment, as opposed to the tensile tests of individual ligaments where the ligaments were preconditioned prior to the tests to failure [30-31]. The assumed initial slack strain needs further clarifications when experimental data showing the influence of the preconditioning is available.

In order to ensure the numerical robustness of the model up to 70 km/h impact, it was necessary to simplify the joint models in the upper limb due to the load concentration at the joints. In contrast, the Pedestrian Crash Data Study database [35] shows only 10 joint injuries out of 858 injuries to the upper limb. This suggests that the concentrated load to the upper limb joints may not be realistic possibly due to the lack of the muscle model in the upper limb and its activation upon impact. The lack of bone fracture representation may have resulted in unrealistic loads to the joints. Further studies are needed to clarify the mechanism of injuries to the upper limb. As the car front-end shape and structure would greatly influence car–pedestrian interactions, further investigation will be needed to ensure numerical robustness of the model against different types of cars.

The addition of the musculature around the back of the knee decreased the peak hyperextension angle of the knee from 39.5 degrees to 29.8 degrees, showing that the contribution of the passive musculature is significant in the hyperextension of the knee in a frontal collision. However, the knee response in hyperextension has not been validated and needs further validations. In addition, the neck model validation used rigid constraint of the bottom of the neck musculature and skin, which may influence the neck stiffness and requires further clarifications in a future study. The rigid foot model may need to be further improved in order for the model to be applicable to various orientation and angle of the ankle upon impact.

V. CONCLUSIONS

A full-body FE model for a pedestrian was developed by combining the upper body and the pelvis and lower limb models developed in previous studies. The modifications were made to the neck, upper limb, thorax, knee, leg and ankle in order to enhance the biofidelity and the numerical robustness of the model. The validation of the biofidelity of the model for the modified components showed good match with the experimental data, suggesting that the model is capable of predicting impact responses to the entire body regions, except the upper limb, where the joint models were simplified to improve the numerical robustness. The impact simulations against a simplified car model representing a stiff front-end structure at 70 km/h showed that the model is capable of calculating pedestrian kinematics up to head contact to the car over the entire impact speed range of real-world accidents.

VI. References

[1] European Enhanced Vehicle-safety Committee. EEVC Working Group 17 Report – Improved test methods to evaluate pedestrian protection afforded by passenger cars, *EEVC*, 1998.

[2] Fredriksson, R., Rosén, E. Integrated Pedestrian Countermeasures - Potential of Head Injury Reduction Combining Passive and Active Countermeasures. *Proceedings of IRCOBI Conference*, 2010, Hanover (Germany).

[3] Wang, J. T. Phase II Plan & Status of the Global Human Body Models Consortium. *SAE Government & Industry Meeting*, 2014, Washington, DC (USA).

[4] Watanabe, R., Katsuhara, T., Miyazaki, H., Kitagawa, Y., Yasuki, T. Research of the Relationship of Pedestrian Injury to Collision Speed,Car-type, Impact Location and Pedestrian Sizes using Human FE model (THUMS Version 4). *Stapp Car Crash Journal*, 2012, 56: 269–321.

[5] Takahashi, Y., Suzuki, S., Ikeda, M., Gunji, Y. Investigation on Pedestrian Pelvis Loading Mechanisms Using Finite Element Simulations. *Proceedings of IRCOBI Conference*, 2010, Hanover (Germany).

[6] Ikeda, M., Suzuki, S., Gunji, Y., Takahashi, Y., Motozawa, Y., Hitosugi, M. Development of an Advanced Finite Element Model for a Pedestrian Pelvis. *Proceedings of 22nd ESV Conference*, 2011, Washington D.C. (USA).

[7] Dokko, Y., Yanaoka, T., Ohashi, K. Validation of Age-specific Human FE Models for Lateral Impact. *Proceedings of SAE World Congress*, 2013, Detroit (USA).

[8] Ito, O., Dokko, Y., Ohashi, K. Development of Adult and Elderly FE Thorax Skeletal Models. *Proceedings of SAE World Congress*, 2009, Detroit (USA).

[9] Bartleby.com. "Henry Gray (1825–1861). Anatomy of the Human Body. 1918." Internet: http://www.bartleby.com/107/indextn3.html, accessed 24 March 2015.

[10] Takahashi, Y., Kikuchi, Y. Biofidelity of test devices and validity of injury criteria for evaluating knee injuries to pedestrians. *Proceedings of 17th ESV Conference*, 2001, Amsterdam (The Netherlands).

[11] Shin, J., Lee, S., et al. Development and validation of a finite element model for the Polar-II upper body. *Proceedings of SAE World Congress*, 2006, Detroit (USA).

[12] National Highway Traffic Safety Administration. Laboratory Test Procedure for FMVSS 208, Occupant Crash Protection Sled Tests, TP-208S-01.

[13] Hadjipanayi, E., Mudera, V., Brown, R. A. Guiding cell migration in 3D: A collagen matrix with graded directional stiffness. *Cell Motility and the Cytoskeleton*, 2009, 66(3):121–8.

[14] Susilo, M. E., Roeder, B. A., Voytik-Harbin, S. L., Kokini, K., Nauman, E. A. Development of a three-dimensional unit cell to model the micromechanical response of a collagen-based extracellular matrix. *Acta Biomaterialia*, 2010, 6(4):1471–86.

[15] Lewis, G., Shaw, K. M. Modeling the tensile behavior of human Achilles tendon. *Bio-Medical Materials and Engineering*, 2012, 7(4): 231–44.

[16] Bertram, J. E., Polevoy, Y., Cullinane, D. M. Mechanics of avian fibrous periosteum: tensile and adhesion properties during growth. *Bone*, 1998, 22(6):669–75.

[17] Institute for Traffic Accident Research and Data Analysis. 2013 Traffic Accident Statistics (in Japanese), 2011.

[18] Bizot, P., Meunier, A., Chrisfel, P., Witvoet, J. Experimental Passive Hyperextension Injuries of the Knee; Biomechanical Aspects of Their Consequences (in French). *Revue de Chirurgie Orthopedique et Reparatrice de L'appareil Moteur*, 1995, 81(3):211–20.

[19] Lloyd, D. G., Buchanan, T. S. Strategies of muscular support of varus andvalgus isometric loads at the human knee. *Journal of Biomechanics*, 2001, 34:1257–67.

[20] Ewing, C., Thomas, D. Human head and neck response to impact acceleration. *NAMRL Monograph*, 1973, 21.

[21] Thunnissen, J., Wismans, J., Ewing, C., Thomas, D. Human Volunteer Head-Neck Response in Frontal Flexion: A New Analysis. *SAE Technical Paper*, 1995, Paper No. 952721.

[22] Kroell, C., Schneider, D., Nahum, A. Impact Tolerance and Response of the Human Thorax. *SAE Technical Paper*, 1971, Paper No. 710851.

[23] Kroell, C., Schneider, D., Nahum, A. Impact Tolerance and Response of the Human Thorax II. *SAE Technical Paper*, 1974, Paper No. 741187.

[24] Eppinger, R. Prediction of Thoracic Injury Using Measurable Experimental Parameters. *Proceedings of the International Conference on Experimental Safety Vehicles*, 1976, London (UK).

[25] Viano, D. Biomechanical Responses and Injuries in Blunt Lateral Impact. *SAE Technical Paper*, 1989, Paper No. 892432.

[26] Ivarsson, J., Lessley, D., et al. Dynamic Response Corridors and Injury Thresholds of the Pedestrian Lower Extremities. *Proceedings of IRCOBI Conference*, 2004, Graz (Austria).

[27] Funk, R., Rudd, R., Kerrigan, J., Crandall, J. Analysis of Tibial Curvature, Fibular Loading, and the Tibia Index. *Proceedings of IRCOBI Conference*, 2003, Lisbon (Portugal).

[28] Takebe, K., Nakagawa, A., Minami, H., Kanazawa, H., Hirohata, K. Role of the fibula in weight-bearing. *Clin. Orthop. Relat. Res.*, 1984, 184:289–92.

[29] Shuler, F., Dietz, M. *Tibial and Fibular Shaft Fractures*. In Essential Orthopaedics, p. 703, *Elsevier*, Philadelphia, USA, 2009.

[30] Bose, D., Sanghavi, P., Kerrigan, J., Madeley, N., Bhalla, K., Crandall, J. Material Characterization of Ligaments Using Non-contact Strain Measurement and Digitization. *International Workshop on Human Subjects for Biomechanical Research*, 2002, Ponte Vedra Beach (USA).

[31] van Dommelen, J., Ivarsson, B., et al. Characterization of the Rate-Dependent Mechanical Properties and Failure of Human Knee Ligaments. *Proceedings of SAE World Congress*, 2005, Detroit (USA).

[32] Bose, D., Bhalla, K., Rooij, L., Millington, S., Studley, A., Crandall, J. Response of the Knee Joint to the Pedestrian Impact Loading Environment. *Proceedings of SAE World Congress*, 2004, Detroit (USA).

[33] Crandall, J., Portier, L., et al. Biomechanical Response and Physical Properties of the Leg, Foot, and Ankle. *SAE Technical Paper*, Paper No. 962424, 1996.

[34] Asanuma, H., Takahashi, Y., Ikeda, M., Yanaoka, T. Investigation of a Simplified Vehicle Model that Can Reproduce Car-Pedestrian Collisions. *Proceedings of SAE World Congress*, 2014, Detroit (USA).

[35] National Highway Traffic Safety Administration. National Automotive Sampling System, Pedestrian Crash Data Study, 1994–1998.

VII. APPENDIX

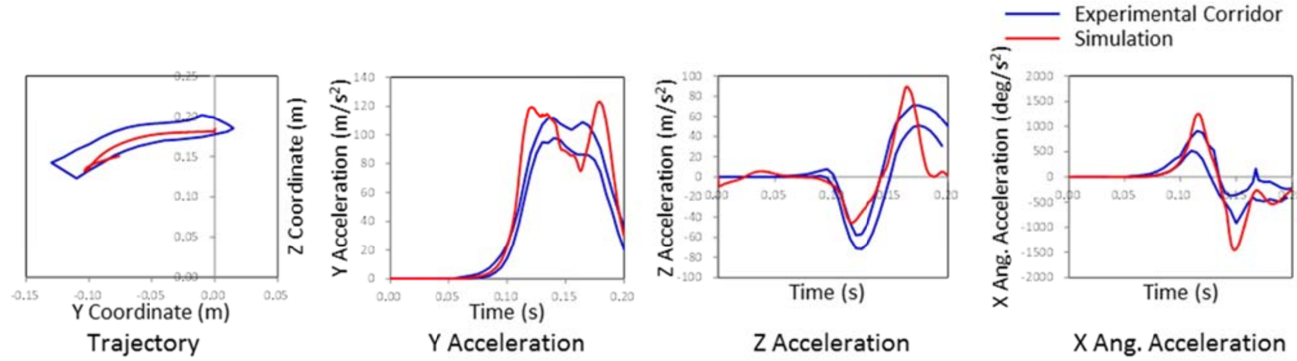

Fig. A1. Head-neck response validation results in lateral bending.

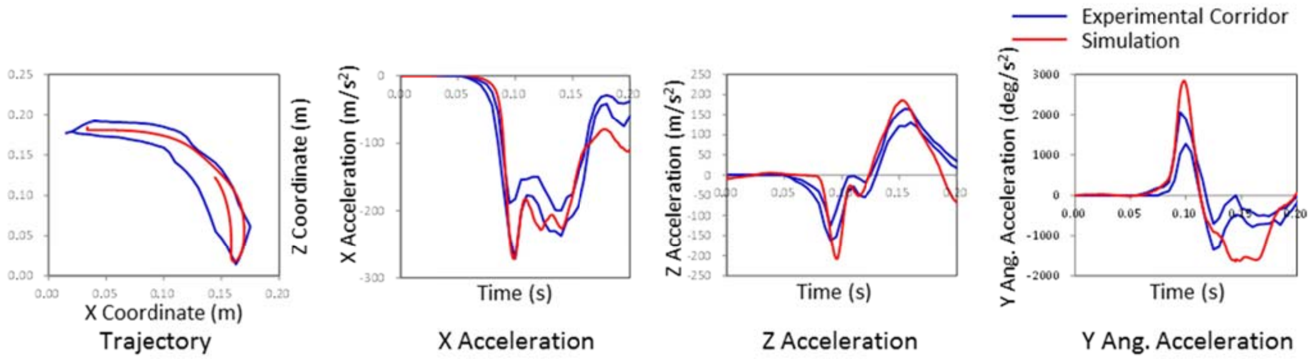

Fig. A2. Head-neck response validation results in flexion.

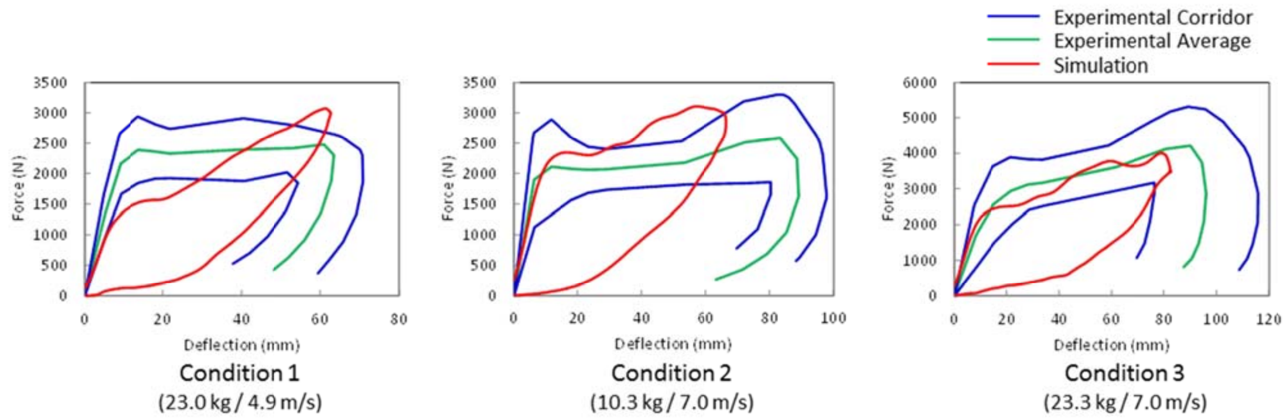

Fig. A3. Validation results of frontal thoracic impact.

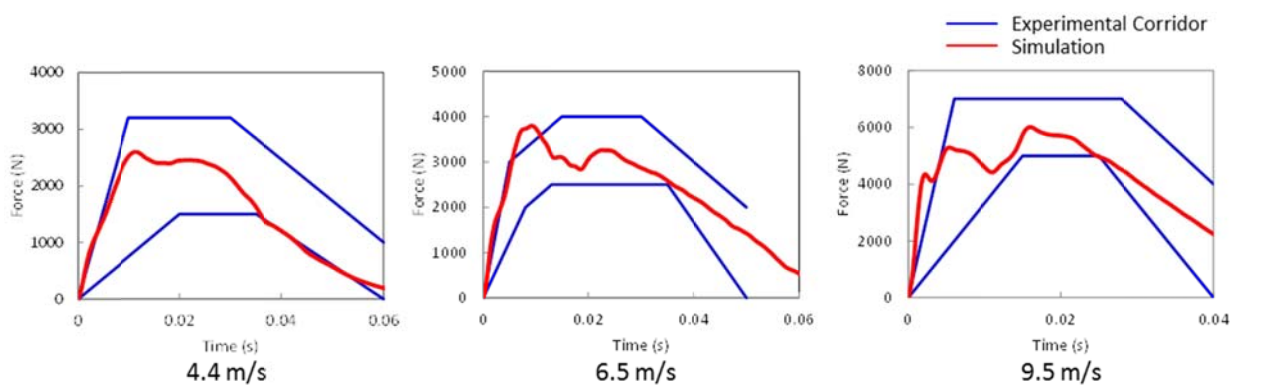

Fig. A4. Validation results of oblique thoracic impact.

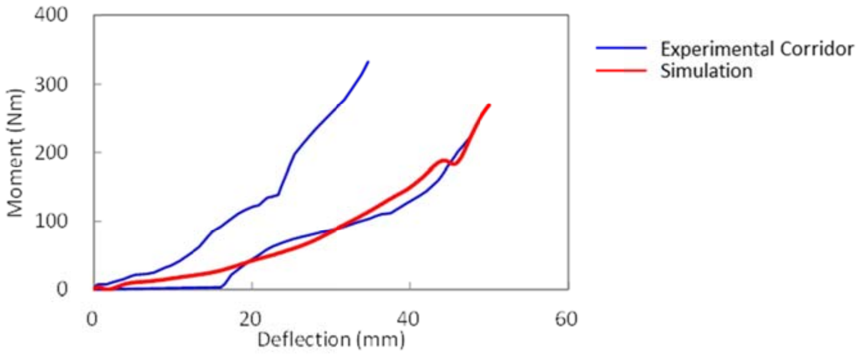

Fig. A5. Validation results of leg 3-point bending.

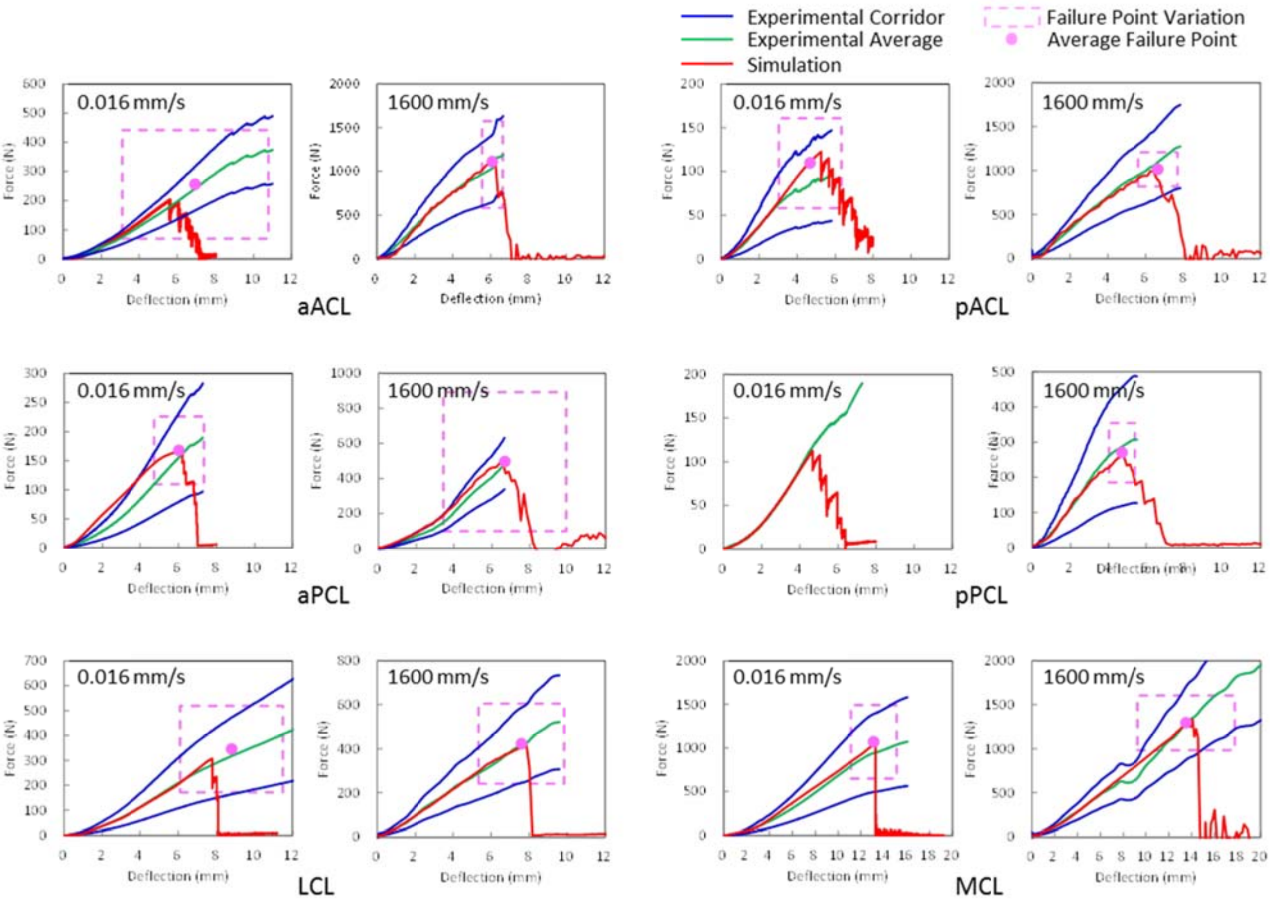

Fig. A6. Validation results of individual knee ligament bundles in tension.

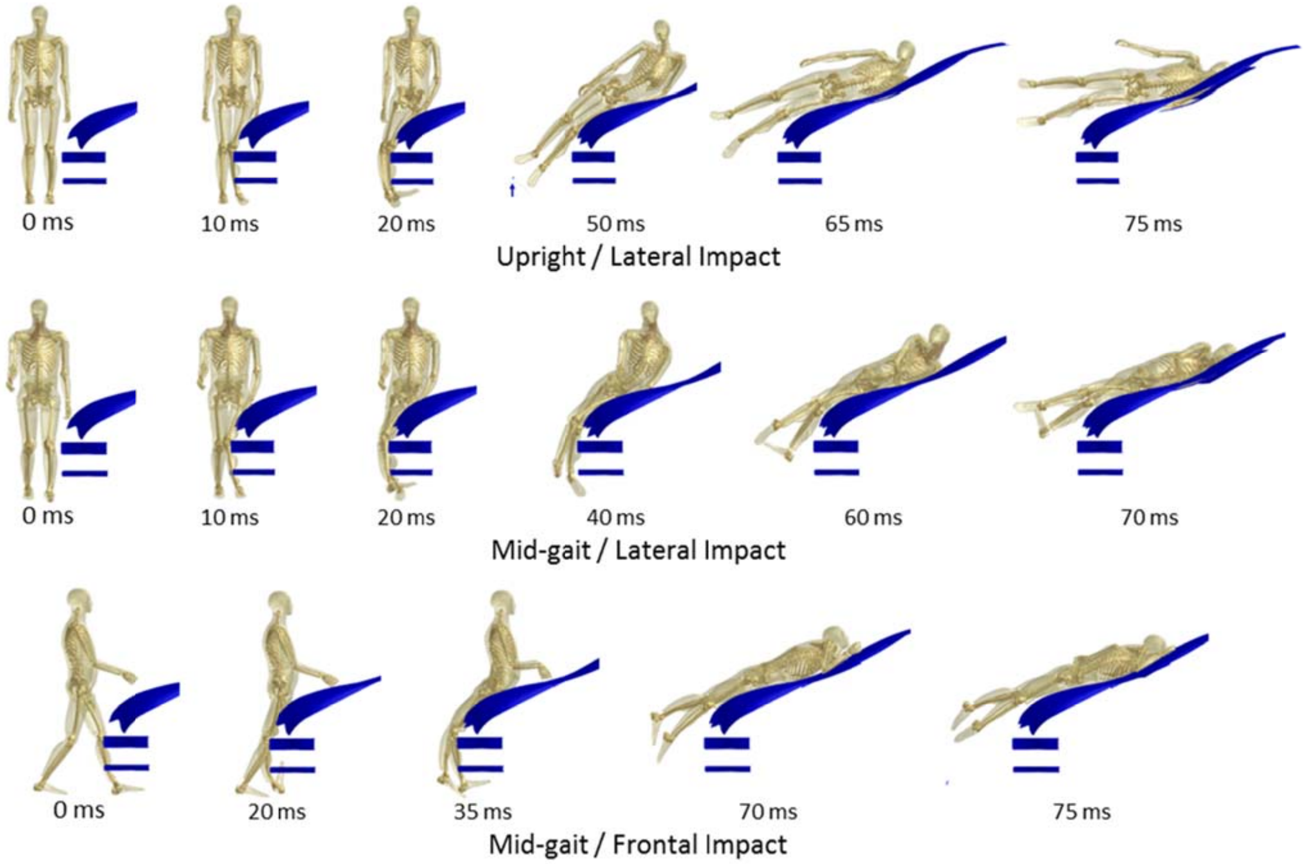

Fig. A7. Kinematics of pedestrian model during impact from simplified car model at 70 km/h.